

Article

Simulation of the Circulating Bearing Currents for Different Stator Designs of Electric Traction Machines

Yusa Tombul , Philipp Tillmann  and Jakob Andert * 

Teaching and Research Area Mechatronics in Mobile Propulsion, Faculty of Mechanical Engineering, RWTH Aachen University, Forckenbeckstraße 4, 52074 Aachen, Germany; tombul@mmp.rwth-aachen.de (Y.T.); philipp.tillmann@rwth-aachen.de (P.T.)

* Correspondence: andert@mmp.rwth-aachen.de

Abstract: Pulse-width modulated inverters are commonly used to control electrical drives, generating a common mode voltage and current with high-frequency components that excite the parasitic capacitances within electric machines, such as permanent magnet synchronous machines or induction machines. This results in different types of bearing currents that can shorten the service life of electric machines. One significant type of inverter-induced bearing currents are high-frequency circulating bearing currents. In this context, this work employs finite element analysis and time-domain simulations to determine the common mode current and circulating bearing current for various permanent magnet synchronous machine designs based on the traction machines of commercial electric vehicles with a focus on the stator. The results suggest that the ratio between the circulating bearing current and common mode current is much smaller in permanent magnet synchronous machines for traction applications than previously established in conventional induction machines, with values below 10% for all analyzed designs. A further increase in the robustness of such electric machines to the detrimental effects caused by the inverter supply could be achieved by reducing the parasitic winding-to-stator capacitance or by increasing the stator endwinding leakage inductance.

Keywords: bearing currents; common mode current; electric traction machines; finite element analysis; permanent magnet synchronous machine



Citation: Tombul, Y.; Tillmann, P.; Andert, J. Simulation of the Circulating Bearing Currents for Different Stator Designs of Electric Traction Machines. *Machines* **2023**, *11*, 811. <https://doi.org/10.3390/machines11080811>

Academic Editor: Juan Carlos Travieso-Torres

Received: 30 June 2023

Revised: 30 July 2023

Accepted: 2 August 2023

Published: 7 August 2023



Copyright: © 2023 by the authors. Licensee MDPI, Basel, Switzerland. This article is an open access article distributed under the terms and conditions of the Creative Commons Attribution (CC BY) license (<https://creativecommons.org/licenses/by/4.0/>).

1. Introduction

Most variable-speed electrical drives consist of a three-phase voltage source inverter (VSI) and an electric machine, with the latter usually being a squirrel-cage induction machine in conventional industrial applications, or a permanent magnet synchronous machine (PMSM) in areas where efficiency and power density are a major concern, for example in the automotive and aircraft sectors. Their various control algorithms, such as field-oriented control, model predictive control, adaptive control, sliding mode control and H-infinity control include pulse-width modulation (PWM) of the VSI. This leads to non-sinusoidal phase-to-ground voltages displaying a pulse-shaped waveform with steep rise and fall slopes, generating a parasitic common mode (CM) voltage u_{CM} , defined as the arithmetic average of these phase-to-ground voltages [1]. The CM voltage amplitude and frequency are proportional to the inverters DC-link voltage and switching frequency, respectively.

Within an electric machine, several parasitic capacitances exist due to the separation of a pair of electrodes by an insulating medium. The largest one is the winding-to-stator capacitance C_{ws} , shown in Figure 1a, originating from the separation of the stator windings and stator iron core by the winding insulation, slot insulation and impregnation [2]. This capacitance causes a CM current i_{CM} to flow at each inverter switching transition because of the change in the CM voltage. The CM current enters the electric machine through the windings, transitions through C_{ws} to each individual sheet of the stator lamination stack

and exits through the grounding cable connected to the machine housing [3]. Due to the pronounced skin effect resulting from the high oscillation frequency of the CM current, it flows along the surface of each lamination sheet and proceeds axially between sheets through the housing. In the process, as depicted in Figure 1b, the CM current excites a CM flux ϕ_{CM} around and along the machine shaft, resulting in an induced shaft end-to-end voltage u_{sh} , which causes a high-frequency (HF) circulating bearing current i_b to flow at each inverter switching transition either at low rotational speeds, i.e., when the bearings are in a conductive state due to a thin lubricant film separating the bearing races and rolling elements, or when the shaft end-to-end voltage exceeds the lubricant film breakdown voltage [3,4]. The circulating bearing current flows in the loop formed by the electric machine housing, stator lamination stack, both bearings, rotor lamination stack and the shaft. It has the same waveform and amplitude but opposite polarity on both bearings.

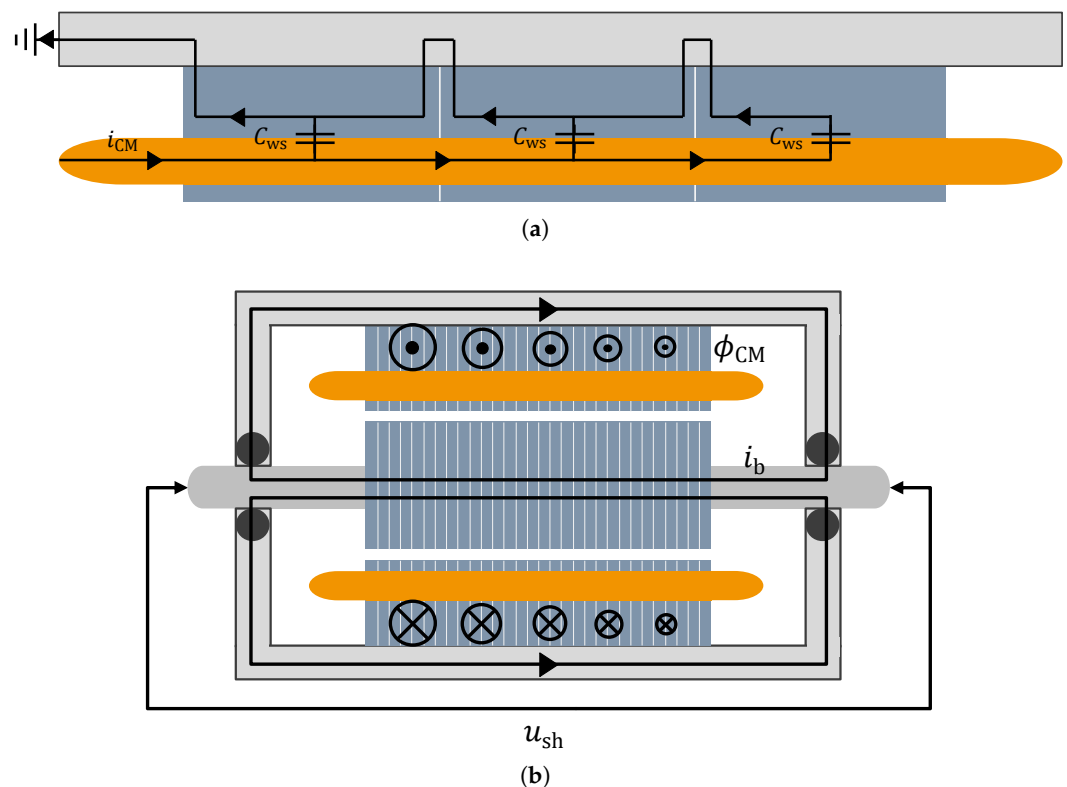


Figure 1. Schematic representation of the (a) CM current i_{CM} and (b) circulating bearing current i_b flow in an electric machine. The flow path of i_b is simplified [3].

Although previous publications [1,5] analyzed the influence of stator design variations on the bearing voltage responsible for causing electric discharge machining bearing currents simulatively, similar studies pertaining to the circulating bearing currents have not been published yet according to the knowledge of the authors. References [3,4,6] contain measurement data that were obtained from induction machines and PMSMs of different frame sizes and power ratings, but apart from these specifications, few design parameters were listed, particularly for the induction machines. Furthermore, these studies focused on conventional industrial applications and knowledge of electric vehicle traction machines regarding their exposure to bearing currents is still very limited.

Therefore, this work aims to compare different electric traction machine designs based on the PMSMs of commercially available electric vehicles with regards to circulating bearing currents by way of finite element analysis (FEA) and time-domain simulations. Section 2 describes the considered designs with both hairpin and stranded winding variations, followed by a description of the FEA and time-domain simulation setups. Equations to calculate the bearing current model parameters analytically are also provided in this

section. Section 3 presents the simulation results and contains a discussion pertaining to the influence of the design variations on the CM and bearing currents. Finally, the conclusions are summarized in Section 4, and possible outlooks are given.

2. Materials and Methods

2.1. Analyzed Electric Machine Designs

Eight different electric machine designs based on the PMSMs of commercial electric vehicles were chosen, six of them with hairpin windings and two with stranded or round-wire windings. The focus is on the stator design parameters, whereas the rotor is treated as a circle, and only its inner and outer diameters are considered for the analysis.

The most important specifications of the analyzed designs pertaining to the circulating bearing current determination are listed in Tables 1 and 2, respectively. According to the number of winding layers per slot, the designs with hairpins are termed H2, H4, H6 and H8, and the ones with stranded wires, S1 and S2. The hairpin variations with four and eight layers also differentiate between front (F) and rear (R) electric machine designs, originating from their placement in electric vehicles with separate front and rear wheel drives. The H8 designs differ mainly in the lamination stack length and emphasize the influence of this parameter on the bearing currents. The airgap is roughly 1 mm for all designs, which is why the stator inner diameter is not listed explicitly.

Table 1. Specifications of the analyzed electric traction machine designs with hairpin winding.

Parameter	H2	H4 F, R	H6	H8 F, R
Stack length/mm	175	160, 210	175	91, 156
Lamination sheet thickness/mm	0.35	0.28	0.27	0.25
Stack-to-housing distance/mm	120	0	81	84.1, 56.2
Rotor inner diameter/mm	47	60	63	50
Rotor outer diameter/mm	133	130, 171	161	132
Stator outer diameter/mm	190	190, 243	220	200
Slot-pole ratio	48/8	72/8	48/8	48/8
Slot height/mm	15.2	16.5, 14	14.7	16.2
Slot width/mm	5.1	3.25, 3.6	6.8	3.5
Conductor height/mm	5.7	3.3, 2.65	1.5	1.4
Conductor width/mm	4.3	2.4, 2.85	6.2	2.8
Slot fill factor/%	70.7	67.2, 70	68	61.3

Some parameters with dimensions below 1 mm could also vary between the analyzed designs and even within the same design due to production tolerances. Here, these parameters are chosen as follows:

- The slot insulation thickness is 0.2 mm for all hairpin designs and listed separately for the stranded winding designs in Table 2.
- The wire insulation thickness is 0.1 mm for hairpins and 0.033 mm for stranded wires.
- The distance between the insulation layers of adjacent wires is 0.1 mm with the exceptions of H2 and S1, where 0.5 mm and 0.05 mm are assumed, respectively.
- Due to a lack of detailed material information, the lamination stack of all considered designs is assumed to consist of the same sheet material with a relative permeability of 900 at 50 Hz, an electrical conductivity of 1.92 MS/m and a stacking factor of 0.97.

Table 2. Specifications of the analyzed electric traction machine designs with stranded winding.

Parameter	S1	S2
Stack length/mm	135	135
Lamination sheet thickness/mm	0.3	0.3
Stack-to-housing distance/mm	61	92
Rotor inner diameter/mm	53	70
Rotor outer diameter/mm	130	150
Stator outer diameter/mm	200	225
Slot-pole ratio	48/8	54/6
Slot height/mm	20	18.9
Tooth width/mm	5.3	4.35
Slot insulation thickness/mm	0.25	0.4
Number of wires per slot/mm	62	61
Conductor diameter/mm	0.87	0.81
Slot fill factor/%	45	38

2.2. Finite Element Analysis

Electrostatic FEA was utilized in the simulation environment Ansys Electronics Desktop (AEDT) with the application Q2D extractor to determine the winding-to-stator capacitance C_{ws} , which is introduced in Section 1 and shown in Figure 1a. Based on the results from references [6,7], where three-dimensional FEA was used to compute the components of C_{ws} within the slots and in the endwindings separately, the endwinding component was considered negligible here, and only two-dimensional FEA was employed. Moreover, Kindl et al. [8] compared two-dimensional FEA simulation results with measurements of the parasitic capacitances in an electric machine with form-wound windings. It was shown that for such winding arrangements, the accuracy of FEA can be very high with deviations below 2 % for C_{ws} in particular. Similar accuracy is expected for the hairpin designs.

For stator windings consisting of stranded wires, the FEA is more susceptible to deviations due to the distance of the wires towards the stator core, which can significantly influence the value of C_{ws} [9]. In reality, this distance differs between slots and even within the same slot of an electric machine. This was taken into account by using a randomization algorithm on all wires. The algorithm first distributes horizontal lines along the slot height, starting from a predefined position at the slot bottom and ending at the slot top with distances of one wire diameter (conductor and insulation) plus the predefined wire-to-wire distance between each horizontal line. In the next step, it iteratively distributes the maximum number of wires that does not cause intersection with the slot insulation along the lines, whereas the wires of each subsequent layer are shifted by one wire radius along the line length, causing an alternating number of wires per layer, which increases towards the slot top due to the trapezoidal shape of slots containing stranded wires. Once all conductor layers have been filled and the number of placed wires exceeds the given number of wires per slot (see Table 2), the ones that were added last are removed again. Afterwards, the randomization iteratively defines a hexagon around each wire and moves the wire by a predefined distance in one of the six possible directions. If this movement causes an intersection with another wire or the slot insulation, it is repeated until no intersections occur.

Figure 2 shows the radial view of a single slot pitch for all analyzed designs in the AEDT environment. Comparing the stranded wire designs, it can be seen that for S1, the randomization leads to less variation among wires, especially for the wires not adjacent to the slot insulation because of the small inter-wire distance. For setting up the electrostatic FEA simulations, the following assumptions and simplifications have been made:

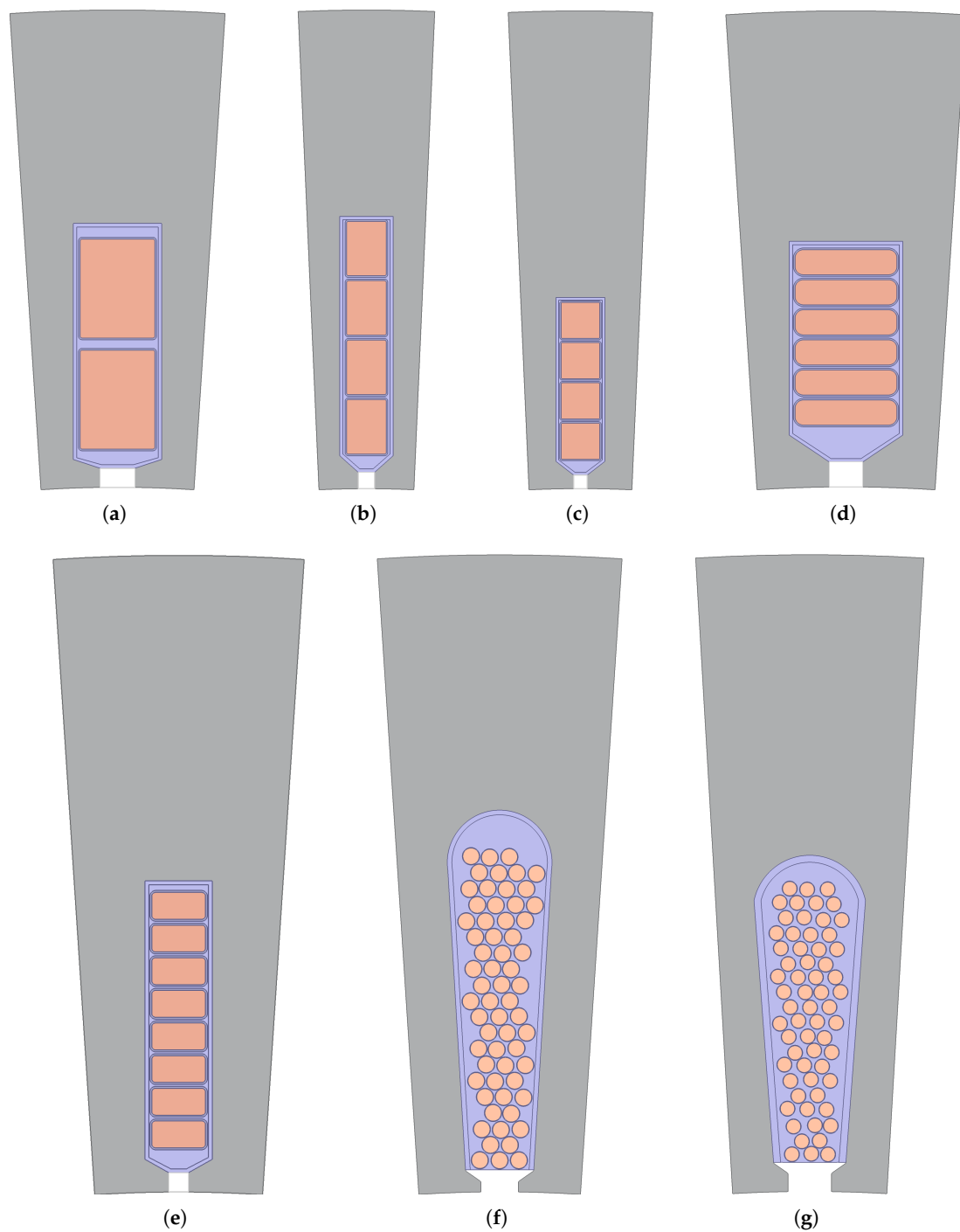


Figure 2. Radial view of a single slot pitch of the analyzed designs in Ansys Electronics Desktop (AEDT): (a) H2, (b) H4 F, (c) H4 R, (d) H6, (e) H8 F/R, (f) S1, (g) S2.

- The stator slot area outside of the windings consists of impregnation material.
- All designs have the same insulation materials with their relative permittivities, considered independent of the frequency and temperature, listed in Table 3.
- The hairpins are ideally centered within the stator slots.
- The influence of direct oil cooling on C_{ws} was neglected. Kim et al. [10] analyzed how direct oil cooling may affect the parasitic capacitances within an electric machine.

Table 3. Chosen relative permittivities of insulation materials.

Component	Relative Permittivity
Slot insulation	2.7
Winding insulation	3
Impregnation	3.3

2.3. Time-Domain Simulations

The time-domain simulations were performed in Matlab/Simulink with the toolbox Simscape Electrical. In the following subsections, the models of the VSI and electric machine are described in more detail.

2.3.1. Voltage Source Inverter Model

Figure 3 depicts the schematic of the VSI model as it was built in the Simulink environment. The presented approach omits a physical representation of the inverters power semiconductor devices and parasitics and instead generates the phase-to-ground output voltages with respect to the DC-link midpoint directly within the signal domain by scaling the PWM signals with half of the DC-link voltage U_{DC} and adjusting the rise and fall slopes with a rate-limiter block [11]. For a design-specific comparison of the CM and circulating bearing currents among the considered electric machines independent of the inverter operating conditions, the DC-link voltage was set to 400 V for all simulations. The slew rate $\frac{du}{dt}$ of rise and fall slopes was set to 2.5 V/ns. This relatively low value was deliberately chosen to enable a validation of the presented simulation results with test bench measurements without the availability of a fast switching inverter based on wide-bandgap semiconductor devices. Sinusoidal PWM was implemented by generating sinusoidal reference signals with a constant modulation index of 0.9 and comparing them to a triangular carrier signal with a switching frequency of 8 kHz. The fundamental electrical frequency of the sinusoidal reference signals was set to 40 Hz, corresponding to a rotational speed of 600 rpm and 800 rpm for the designs with eight and six poles, respectively. The reason for this is that circulating bearing currents tend to occur at low rotational speeds, where the bearing lubricant is not fully distributed between the races and rolling elements.

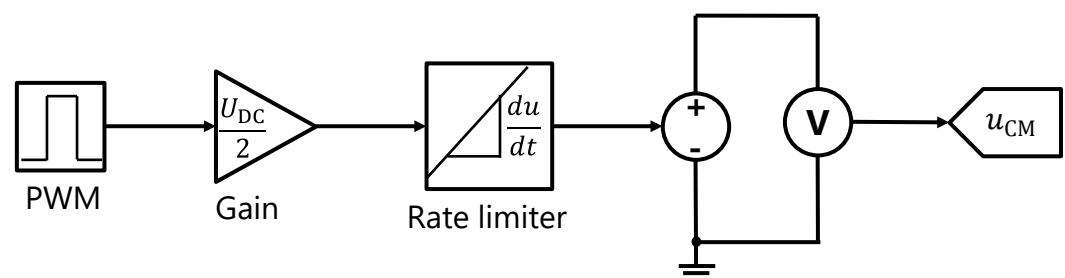
**Figure 3.** Schematic of the inverter model implementation in Simulink.

Figure 4 shows the resulting plot of the CM voltage u_{CM} over two periods, obtained from the arithmetic average of the phase-to-ground voltages. It transitions between $\pm U_{DC}/2 = 200$ V and $\pm U_{DC}/6 \approx 66.7$ V with steps of $\pm U_{DC}/3 \approx 133.3$ V. The limited $\frac{du}{dt}$ of the voltage transitions is not visible in Figure 4. Since the modeling of AC cables interconnecting the inverter and electric machine was omitted due to the structure of electric vehicle drive units, where the latter two components are kept in close proximity to each other, no voltage overshoots or oscillations are present in the CM voltage.

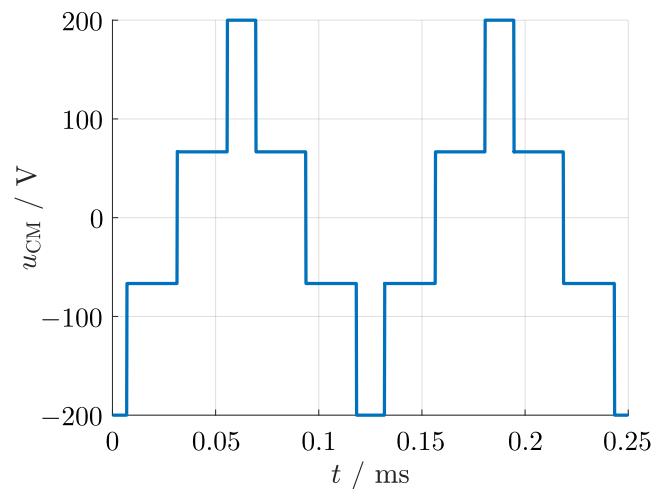


Figure 4. Simulated common mode (CM) voltage.

2.3.2. Electric Machine Model

The equivalent circuit diagram of the electric machine for the simulation of the CM and HF circulating bearing current is shown in Figure 5. The input of this circuit is the CM voltage u_{CM} , which is the output of the inverter model. The loop formed by the stator winding resistance R_s , the stator leakage inductance L_s , winding-to-stator capacitance C_{ws} , grounding resistance R_g and stator-to-ground impedance $Z_{g,s}$ determines the CM current i_{CM} . The CM current usually oscillates with frequencies between 100 kHz and 1 MHz [2], leading to a pronounced skin effect, which increases resistance and decreases inductance [12]. Thus, R_s was calculated analytically with the equations given in [13] at a constant temperature of 100 °C for all designs while considering the increase through the skin effect factor. The skin effect is more pronounced within the slots than in the endwindings, which is why at high frequencies, the endwinding leakage inductance becomes the dominant component of the total stator leakage inductance L_s [13,14]. This parameter was calculated with the equation given in [15]. The grounding resistance R_g is the resistance that the CM current experiences on its path towards ground through the electric machine housing and the grounding cable. A constant value of 1 Ω independent of the respective electric machine design was chosen for this parameter.

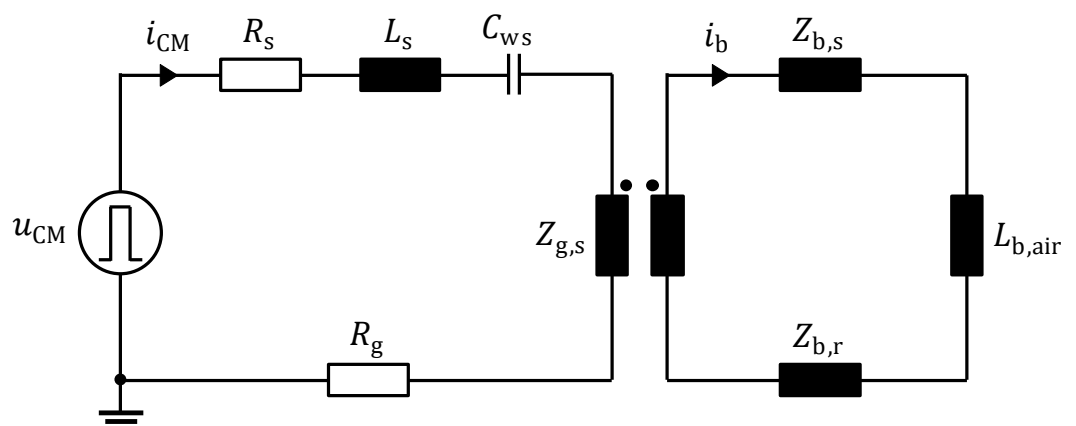


Figure 5. Equivalent circuit diagram of the electric machine for circulating bearing current simulation.

The frequency for the calculation of the skin depth was set to the oscillation frequency of the respective design's CM current, which results from the following equation:

$$f_{res} = \frac{1}{2\pi \cdot \sqrt{L_s \cdot C_{ws}}} \quad (1)$$

For the circulating bearing current i_b , the current transformer circuit on the right loop of Figure 5 is based on [3] by neglecting the small bearing resistances. The stator-to-ground impedance $Z_{g,s}$, mutual to both current loops, was calculated with Equations (2) and (3):

$$Z_{g,s} = R_{g,s} + j\omega_{res} \cdot L_{g,s} = (1 + j) \cdot \frac{\omega_{res} \cdot N_{Fe} \cdot \mu_0 \cdot \mu_{Fe} \cdot \delta_{Fe}}{4\pi} \cdot \ln\left(\frac{D_{s,o}}{D_{s,i} + 2 \cdot h_s}\right) \quad (2)$$

$$\delta_{Fe} = \frac{1}{\sqrt{\pi \cdot f_{res} \cdot \mu_0 \cdot \mu_{Fe} \cdot \sigma_{Fe}}} \quad (3)$$

where δ_{Fe} is the skin depth of the CM current in the lamination sheets, μ_0 the magnetic constant, μ_{Fe} and σ_{Fe} the relative permeability and electrical conductivity of the lamination sheet material, respectively, $\omega_{res} = 2\pi \cdot f_{res}$ the angular oscillation frequency of the CM current, N_{Fe} the number of lamination sheets which can be calculated from the stack length and sheet thickness, $D_{s,i}$ and $D_{s,o}$ the stator inner and outer diameter, respectively, and h_s the slot height.

$Z_{b,s}$ is the impedance of the circulating bearing current through the stator lamination stack, where it flows along the surface of each lamination sheet and proceeds axially through the housing. $Z_{b,s}$ is equal to twice the stator-to-ground impedance $Z_{g,s}$ [4]. $L_{b,air}$ is the airgap and endwinding cavity inductance, calculated according to Equation (4), where l_{Fe} is the lamination stack length, l_b the distance between the housing and stack (see Tables 1 and 2), and $D_{r,i}$ and $D_{r,o}$ the rotor inner and outer diameter, respectively.

$$L_{b,air} = \frac{\mu_0}{2\pi} \cdot \left[l_{Fe} \cdot \ln\left(\frac{D_{s,i}}{D_{r,o}}\right) + (l_b - l_{Fe}) \cdot \frac{D_{s,o}}{D_{r,i}} \right] \quad (4)$$

Schuster et al. [6] performed bearing current measurements on two PMSMs with the same power rating of 90 kW but different dimensions. They displayed lower values compared to the induction machines of previous studies [3,4]. This is likely due to the lack of an electrically conducting rotor cage in PMSMs, which alters the flow path through the rotor lamination stack, leading the current to flow through each lamination sheet as is the case in the stator. This is considered in the rotor impedance $Z_{b,r}$ in Figure 5, which is not assumed to be equal to the stator impedance $Z_{b,s}$ as assumed in [7], but instead calculated with Equation (5), which is based on Equation (2) by replacing the stator diameters and the slot height within the logarithm with the rotor diameters. Since the ratio between the rotor outer and inner diameter is larger than that between the stator outer diameter and the yoke diameter, $Z_{b,r}$ becomes the largest impedance in the bearing current flow path.

$$Z_{b,r} = R_{b,r} + j\omega_{res} \cdot L_{b,r} = (1 + j) \cdot \frac{\omega_{res} \cdot N_{Fe} \cdot \mu_0 \cdot \mu_{Fe} \cdot \delta_{Fe}}{2\pi} \cdot \ln\left(\frac{D_{r,o}}{D_{r,i}}\right) \quad (5)$$

Table 4 lists the parameters of the right loop in Figure 5 that were calculated with Equations (1)–(5), where the stator-to-ground impedance $Z_{g,s}$ and the rotor impedance $Z_{b,r}$ were divided into their resistance and inductance components. The very small values of $L_{b,air}$ for the H4 designs result from the lack of distance between the lamination stack and housing (see Table 1), leading to a zero endwinding cavity inductance (the second term in Equation (4)) which is the dominant component of $L_{b,air}$.

Table 4. Analytically calculated parameters of the circulating bearing current loop for all designs.

Design	$R_{g,s}/\Omega$	$R_{b,r}/\Omega$	$L_{g,s}/nH$	$L_{b,air}/nH$	$L_{b,r}/nH$
H2	0.441	6.613	81.38	97.57	1221
H4 F	0.262	2.875	184.6	0.489	2024
H4 R	0.398	4.397	37.94	0.489	4188
H6	0.281	3.93	200.6	57.02	2808
H8 F	0.342	3.57	99.85	67.53	1044
H8 R	0.43	4.5	232.9	45.37	2435
S1	0.218	2.592	315.6	46.46	1877
S2	0.412	3.686	106.3	59.52	952.4

3. Results and Discussion

3.1. Finite Element Analysis Results

Figure 6 illustrates the lumped spice capacitance matrices of all analyzed designs, simulated in AEDT Q2D extractor by assigning a signal line property to each wire and the reference ground property to the stator core. They are $N \times N$ matrices each, with N being the number of wires per slot. The wire index begins with the wires closest to the slot opening (bottom layer) and ends with those closest to the slot top (top layer). The values of capacitive couplings are displayed by the colorbar in pF, with brighter colors indicating larger capacitance. The diagonal matrix entries represent the capacitance of each respective wire to the stator core, whereas the off-diagonal entries represent the capacitances between wires [16]. Hereafter, these individual capacitances will be referred to as c_{ws} and c_{ww} , respectively.

For the hairpin winding designs, the general trend is that the top layer has the largest c_{ws} due to the large overlap area with the stator core not only at the slot sides but at the top as well. The second largest c_{ws} is between the bottom layer and the stator core. The inter-wire coupling c_{ww} is only significant for the hairpins adjacent to each other. The designs where the conductor width is much larger than the conductor height, i.e., H6 and H8, display larger c_{ww} than c_{ws} with the exception of the top and bottom layers (see Figure 6d–f). This is because wide and short hairpins have more overlap area with adjacent wires than they have with the stator core. This is particularly pronounced for the H6 design, with the conductor width being more than four times larger than the height, thus resulting in inter-wire couplings that even exceed the c_{ws} between the bottom layer and the stator core. With an increasing number of layers, the c_{ws} of each layer decreases due to the decreasing conductor height. This is particularly evident when comparing Figure 6a, displaying values close to 160 pF, with Figure 6e, where the largest capacitance barely exceeds 30 pF.

The same holds true for the designs with stranded windings (Figure 6g,h). Here, mainly the wires closest to the slot boundaries or the stator core contribute to the winding-to-stator capacitance, whereas those in between the outermost wires do not. Since there are more wires adjacent to each other than in the case of hairpin windings, the significant inter-wire coupling capacitances c_{ww} are higher in number. Between the two stranded wire designs, S1 has slightly larger c_{ws} than S2 because of the shorter distance between the wires and the stator core.

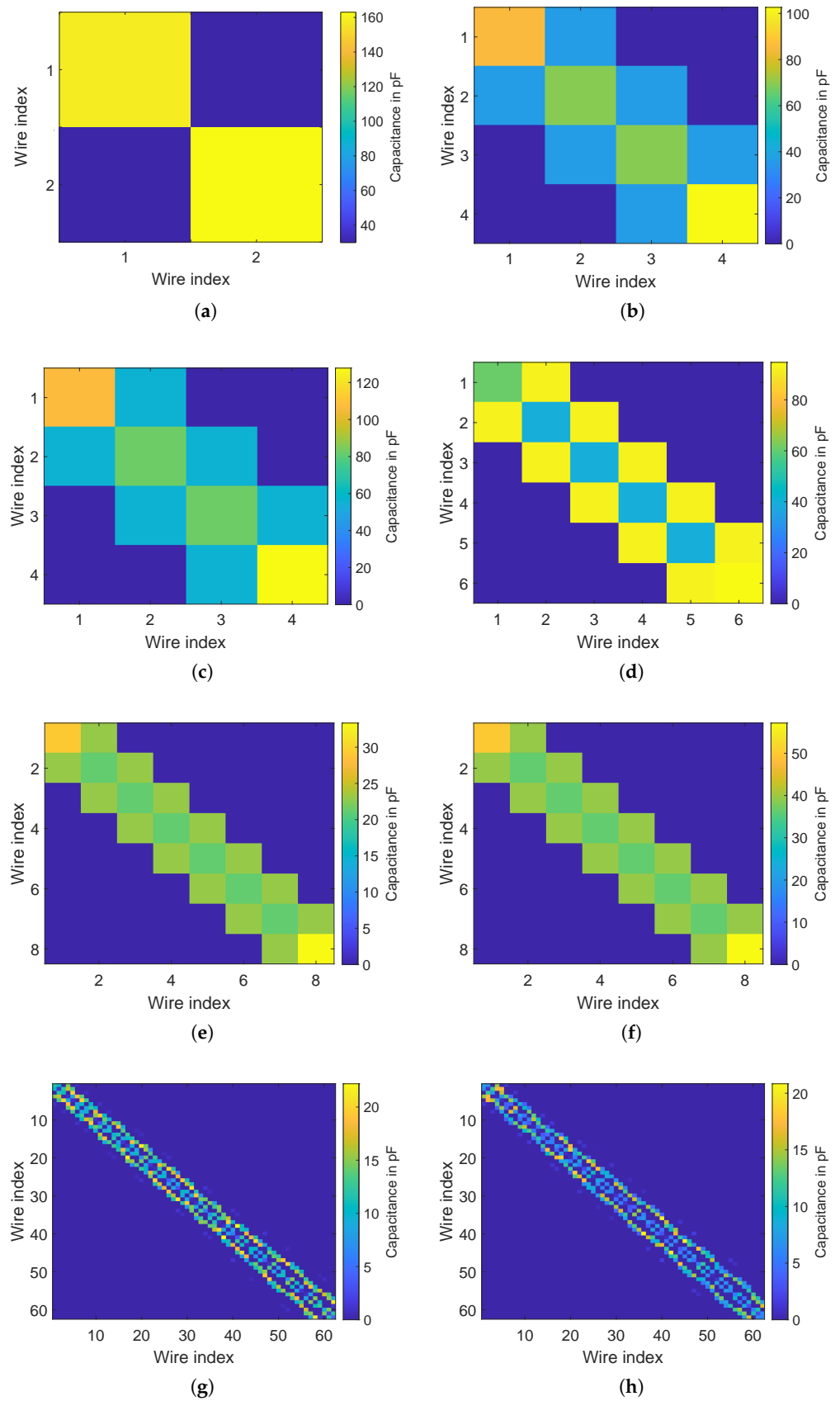


Figure 6. Spice capacitance matrices for the analyzed designs: (a) H2, (b) H4 F, (c) H4 R, (d) H6, (e) H8 F, (f) H8 R, (g) S1, (h) S2.

Table 5 further lists the total winding-to-stator capacitance C_{ws} in nF for all analyzed designs, equal to the sum of the individual c_{ws} for one stator slot multiplied by the number of slots. Also given in the table is the difference between the numerical calculation and an analytical procedure given in references [2,17] for the hairpin winding and stranded winding designs, respectively. Among the hairpin winding designs, H8 F has the smallest C_{ws} by far, and the difference to H8 R originates from the difference in lamination stack length, which scales the capacitance linearly. H2 and H6 have similar capacitance due to the identical stack length, same slot number and similar slot fill factor. However, referring to Figure 2a, the C_{ws} of design H2 is likely to increase if the uppermost wire were to be positioned closer to the slot top. The designs with four layers display the largest C_{ws} mainly due to the higher number of slots, with 72 compared to the 48 slots of other designs. Comparing the numerical results with the analytical values obtained from the equations in [17], it can be seen that the absolute error remains below 10% with the exception of H6, although there is no clear indication as to whether this equation tends to overestimate or underestimate the capacitance value. The identical difference for both H8 designs results from the fact that in the FEA, the wires are positioned identically within the slot.

Table 5. Analytically and numerically calculated winding-to-stator capacitance values.

Design	Numerical C_{ws} /nF	Analytical C_{ws} /nF	Difference/%
H2	15.4	16.02	4.04
H4 F	23.51	25.71	9.36
H4 R	28.8	27.26	−5.33
H6	15.03	13.16	−12.42
H8 F	9.1	8.55	−6.04
H8 R	15.6	14.66	−6.04
S1	10.05	11.1	10.41
S2	7.74	8	3.38

On the other hand, with values around or below 10 nF, the designs with stranded wires exhibit much lower winding-to-stator capacitance C_{ws} than the hairpin winding counterparts (with the exception of H8 F) because of the shorter stack length of 135 mm and less overlap area between the wires and the stator core due to the smaller slot fill factor. Because of the larger fill factor, S1 shows considerably higher C_{ws} than S2 despite having a lower number of stator slots. It should be noted that here, the randomization described in Section 2.2 was only applied to a single slot, and the resulting capacitance was multiplied with the number of slots. To represent a real stranded wire distribution more accurately, the randomization could be applied to every slot individually, but this would also result in a drastic increase in the computational effort. The analytical equation provided in [2] includes form factors to consider that not all of the area around the slot is filled with wires, and the difference to the numerical calculation is similar compared to the hairpin winding cases, with maximum deviations slightly above 10%.

It can be concluded that although there are significant variations in the distribution of individual winding-to-stator and inter-wire couplings, the total C_{ws} is mainly determined by the stack length, slot number and slot fill factor. Among hairpin designs, the number of winding layers is less significant as long as the slot fill factor is similar. Stranded winding designs display lower capacitance values than their hairpin counterparts because of the lower fill factor, even if the stack length was to be the same. Therefore, from a parasitic capacitance standpoint, stranded winding is preferable to hairpin winding.

3.2. Time-Domain Simulation Results

With the numerically determined winding-to-stator capacitance C_{ws} and the analytical calculation of the other model parameters from Figure 5 described in Section 2.3.2, the time-domain simulations were performed in Simulink. The results of the CM current i_{CM} and HF circulating bearing current i_b are displayed in Figures 7 and 8, respectively, over

a time span of 0.25 ms which are two periods of the CM voltage u_{CM} due to the selected switching frequency of 8 kHz (see Figure 4). Each CM voltage transition with positive $\frac{du}{dt}$ leads to a current pulse with positive amplitude and subsequent oscillation, where the oscillation frequency is determined by the resonance frequency f_{res} (see Equation (1)) and its damping by the resistances in the network. This occurs three times each for the transitions with positive and negative $\frac{du}{dt}$ per period of the CM voltage. The respective current amplitudes and the peak-to-peak value of i_b are given in Table 6. Also listed is the ratio between the amplitudes of the circulating bearing current and the CM current, which is termed the bearing current ratio (BCR) in the literature [3]. This ratio can also be calculated analytically via the parameters listed in Table 4 by applying the equation of a current divider.

Table 6. Simulated amplitudes of the CM current, bearing current and bearing current ratio (BCR).

Design	\hat{i}_{CM}/A	\hat{i}_b/A	$\hat{i}_{b,pp}/A$	$\left \frac{\hat{i}_b}{\hat{i}_{CM}} \right / \%$
H2	8.49	0.46	0.733	5.41
H4 F	3.64	0.261	0.428	7.16
H4 R	3.53	0.251	0.421	7.12
H6	2.42	0.141	0.245	5.84
H8 F	2.22	0.161	0.186	7.27
H8 R	2.56	0.189	0.258	7.39
S1	1.81	0.121	0.212	6.66
S2	3.54	0.29	0.525	8.21

Despite not having the largest capacitance C_{ws} , design H2 displays the largest CM current amplitude by far with roughly 8.5 A, which is a factor 2.33 larger than the second largest amplitude shown by design H4 F. This can be attributed to a low number of series-connected winding turns, leading to a much lower stator endwinding leakage inductance compared to the other designs. This leads to a much larger oscillation frequency, visible in Figure 7a, and a smaller impedance at the resonance.

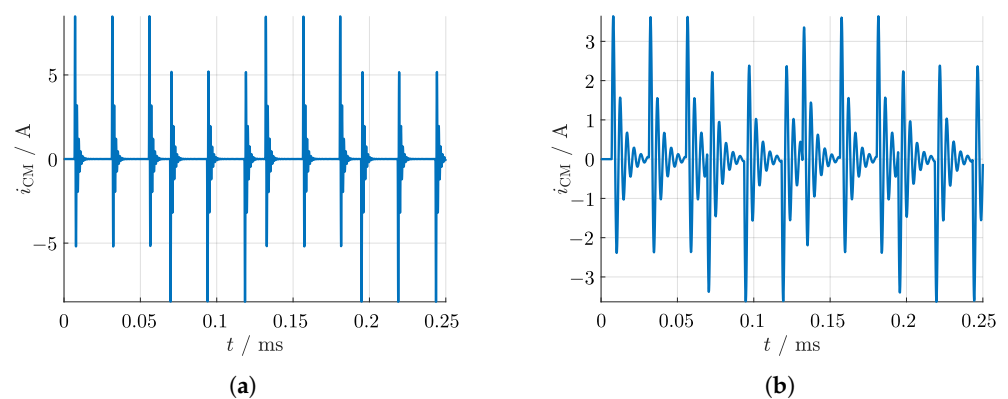


Figure 7. Cont.

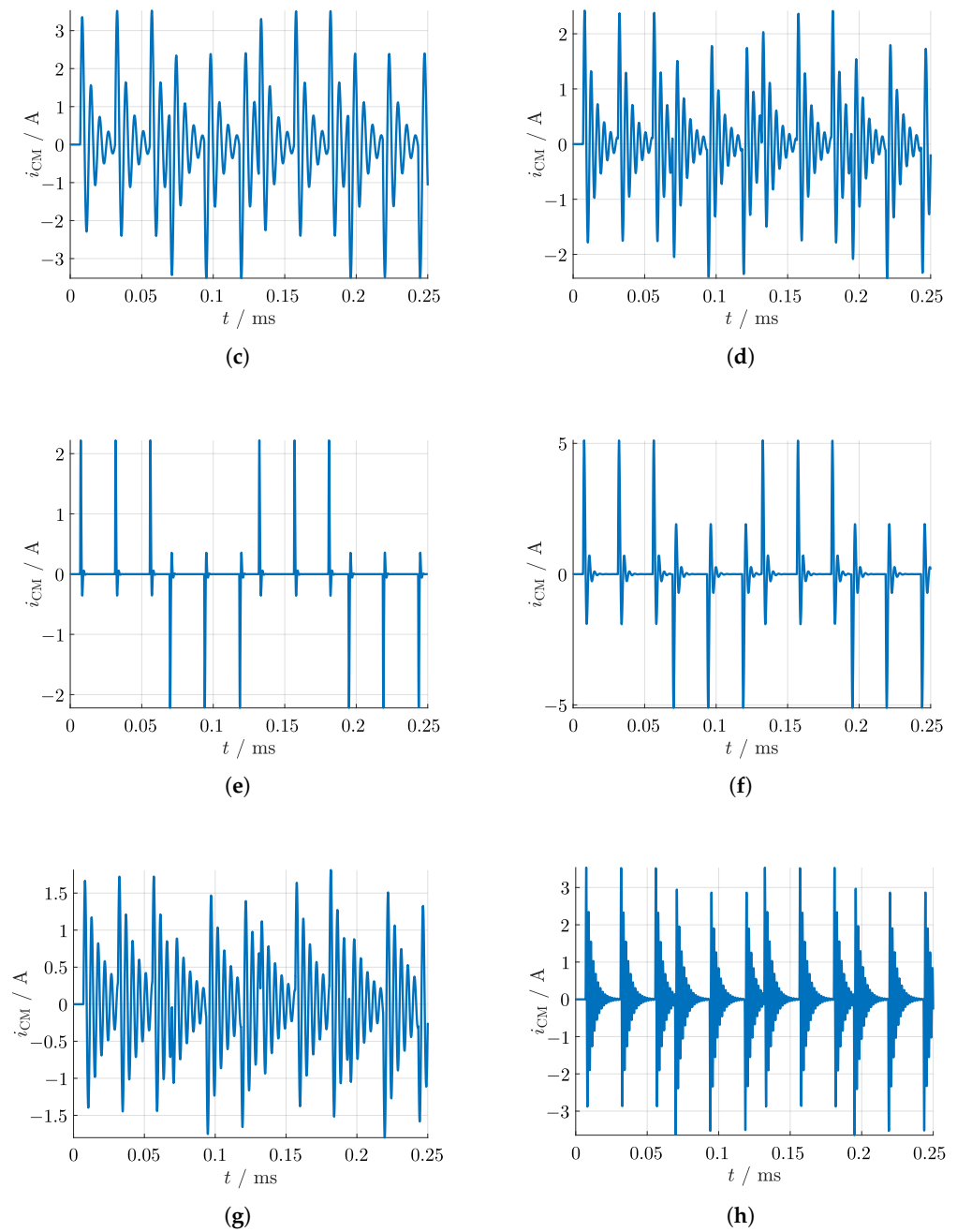


Figure 7. Simulated CM current for the analyzed designs: (a) H2, (b) H4 F, (c) H4 R, (d) H6, (e) H8 F, (f) H8 R, (g) S1, (h) S2.

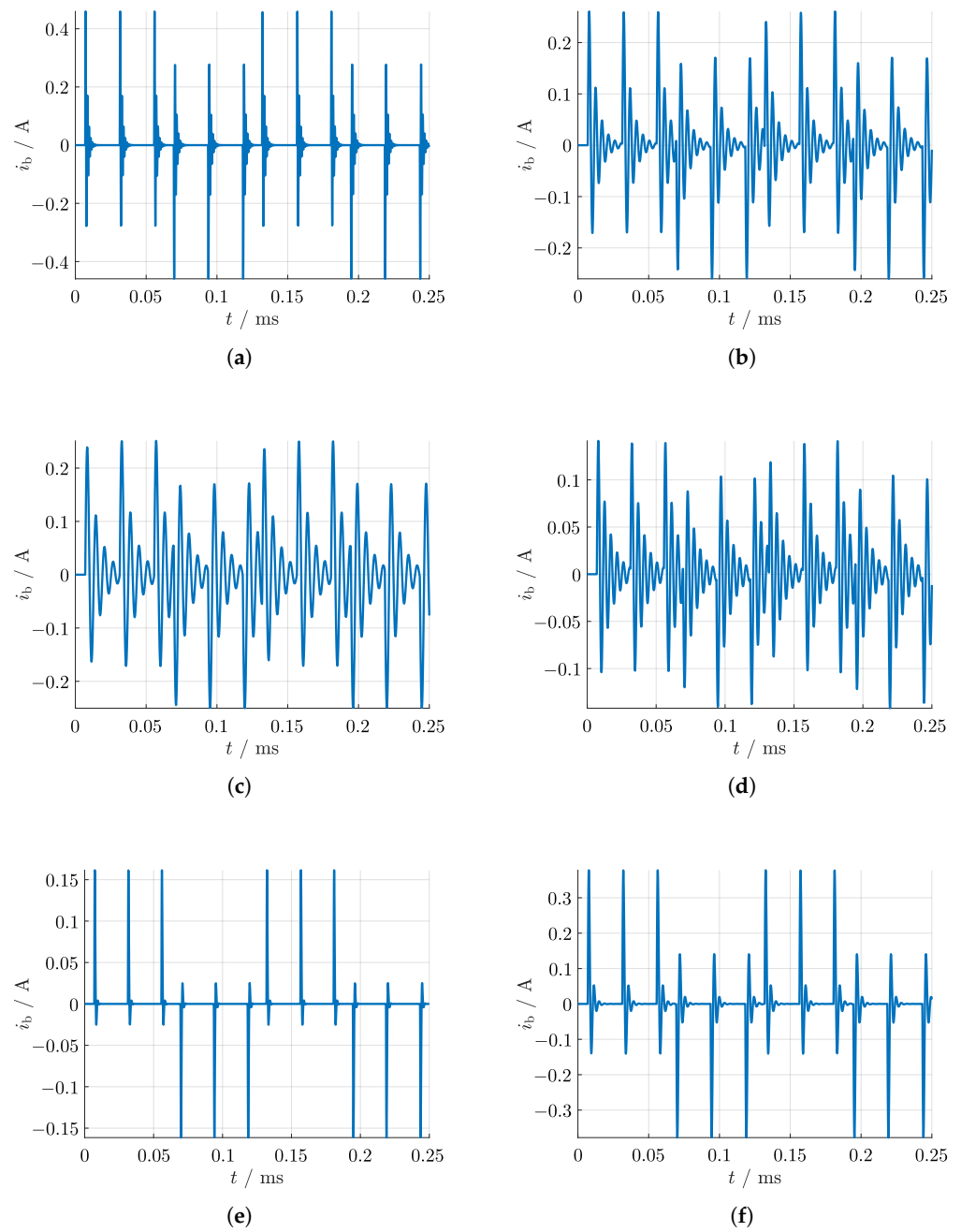


Figure 8. Cont.

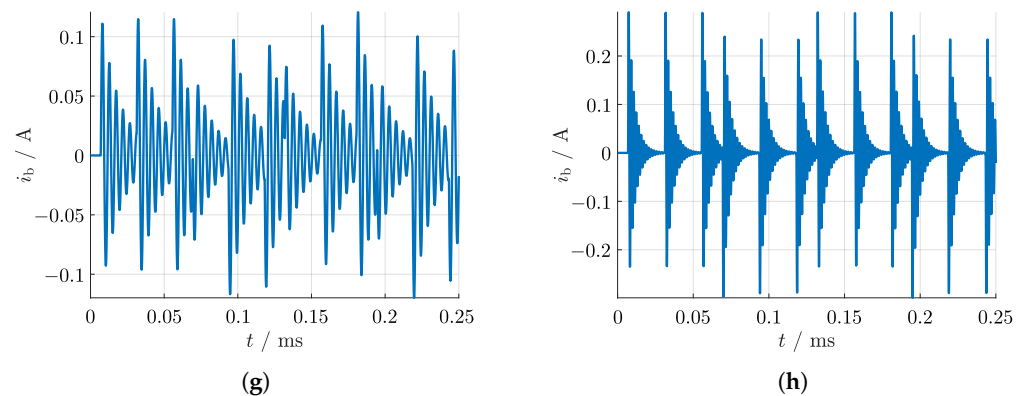


Figure 8. Simulated circulating bearing current for the analyzed designs: (a) H2, (b) H4 F, (c) H4 R, (d) H6, (e) H8 F, (f) H8 R, (g) S1, (h) S2.

This indicates that while not influencing the winding-to-stator capacitance in a significant manner, the number of winding layers still plays a major role in the formation of the CM current. However, design H2 also has the lowest BCR of approximately 5.4%, resulting in a bearing current amplitude of 0.46 A. Despite similar values of the BCR and the capacitance C_{ws} , resulting from the same stack length, same slot number and similar fill factor, the H6 design displays more than three times lower CM and bearing currents. The designs with four hairpin layers display the highest winding-to-stator capacitance by far mainly because of the larger slot number, leading to considerable CM current amplitudes above 3.5 A and bearing current amplitudes above 0.25 A. H4 R has a roughly 22% larger C_{ws} than H4 F, but the 1.5 times larger endwinding leakage inductance leads to slightly smaller values of the CM and bearing currents. The BCR is very similar with values slightly above 7%. The same applies for the designs with eight hairpin layers, where H8 R has a 71% longer stack length and therefore larger C_{ws} but an endwinding leakage inductance that is more than two times larger, altogether leading to similar current amplitudes. Characteristic for these two designs is the much larger damping compared to the other designs, which results from a larger stator winding resistance R_s since the skin effect resistance factor has a quadratic relation to the number of winding layers [13]. This also leads to a lower difference between the bearing current amplitude and its peak-to-peak value.

The stranded winding design S1 has the lowest CM current and bearing current amplitudes, but the relatively weak damping leads to a significant difference between the bearing current amplitude and its peak-to-peak value. Despite having the smallest value of C_{ws} , design S2 displays relatively large current values, which is also due to the smaller value of the endwinding leakage inductance.

Generally, the bearing current waveform closely follows the CM current with relatively low amplitudes ranging from 0.121 A to 0.46 A, which can be attributed to the low BCR ranging from 5.4% to 8.2% for the analyzed PMSMs. This is much lower than previously established for induction machines, where BCRs up to 0.9 have been reported in some cases [3]. Since PMSMs lack a rotor cage, the circulating bearing current is expected to flow through every lamination sheet individually, resulting in a high rotor impedance $Z_{b,r}$. Whether these bearing current values could potentially endanger the bearings of such electric vehicle traction machines has to be investigated by determining the apparent bearing current density, a well-established damage indicator that is the ratio between the peak-to-peak bearing current amplitude and the Hertzian contact area [6]. The latter tends to decrease with smaller bearing size but is also significantly influenced by the applied loads. Since the radial bearing loads are generally larger in automotive applications than the axial loads, this would yield a lower Hertzian contact area and thus larger bearing current density and worse bearing lifetime impairment if a critical value of the bearing current density were to be exceeded.

Considering the relatively similar BCR in the analyzed electric traction machines, a further decrease of the circulating bearing current could be achieved by reducing the CM current. Based on this study, the measures to achieve this could be either a reduction of the winding-to-stator capacitance C_{ws} or an increase of the endwinding leakage inductance L_s . C_{ws} can be reduced by decreasing the lamination stack length or the number of slots. Since the number of slots is fixed by the slot-pole ratio, the remaining possibility would be to shorten the lamination stack at the cost of lower power rating, as was done in the case of the H8 designs. L_s increases with the number of series-connected winding turns. The latter increases with the number of hairpin winding layers and decreases with an increasing number of parallel paths [18].

Finally, it should be noted that the voltage slew rate $\frac{du}{dt}$ of 2.5 V/ns chosen in this study is fairly low, even for inverters with silicon insulated gate bipolar transistors. Some of the analyzed electric traction machines are driven by inverters with wide-bandgap semiconductor devices, capable of much higher switching speeds. Accordingly, the resulting CM current and bearing current amplitudes under such conditions would increase proportionally.

4. Conclusions

Bearing currents are becoming more relevant as a failure cause of electric traction machines in the automotive industry due to the trends towards higher DC-link voltages and faster switching power electronics inverters. However, this phenomenon is still largely unexplored, particularly in this industry. This work employed electrostatic FEA as well as time-domain simulations to study the influence of different stator designs based on the PMSM traction machines of commercial electric vehicles on the HF circulating bearing currents with the aim of finding out the current amplitudes occurring in such designs and their differences in developing these amplitudes.

The analysis yielded that the ratio between the amplitudes of the circulating bearing current and CM current in such PMSMs is much lower than common in induction machines, which have been the focus of bearing current research so far. Moreover, the difference in this ratio between the analyzed designs remains below 3%. Thus, if a further decrease in the circulating bearing currents in PMSMs were to be necessary, for example, due to faster switching inverters, a reduction in the CM current amplitude could be a mitigation strategy. This can be achieved by decreasing the parasitic capacitance between the windings and the stator core or by increasing the stator endwinding leakage inductance.

Future research could focus on increasing the simulation accuracy by including three-dimensional time-harmonic FEA for the endwinding leakage inductance and building a distributed parameter model for the high-frequency behavior of stator windings, as well as experimentally validating the presented results via test bench measurements of the bearing currents on one of the electric traction machines that this study was based on.

Author Contributions: Conceptualization, Y.T.; methodology, Y.T. and P.T.; software, Y.T. and P.T.; validation, Y.T.; formal analysis, Y.T.; investigation, Y.T.; resources, J.A.; data curation, Y.T.; writing—original draft preparation, Y.T.; writing—review and editing, Y.T., P.T. and J.A.; visualization, Y.T.; supervision, Y.T.; project administration, J.A. All authors have read and agreed to the published version of the manuscript.

Funding: This research received no external funding.

Data Availability Statement: All relevant data is presented within the article.

Conflicts of Interest: The authors declare no conflict of interest.

Abbreviations

The following abbreviations are used in this manuscript:

AEDT	Ansys Electronics Desktop
BCR	Bearing current ratio
CM	Common mode
FEA	Finite element analysis
HF	High-frequency
PMSM	Permanent magnet synchronous machine
PWM	Pulse-width modulation
VSI	Voltage source inverter

List of Symbols

C_{ws}	Winding-to-stator capacitance.
$D_{r,i}$	Rotor inner diameter.
$D_{r,o}$	Rotor outer diameter.
$D_{s,i}$	Stator inner diameter.
$D_{s,o}$	Stator outer diameter.
$L_{b,air}$	Airgap and endwinding cavity inductance.
L_s	Stator leakage inductance.
N_{Fe}	Number of lamination sheets.
R_g	Grounding resistance.
R_s	Stator winding resistance.
U_{DC}	DC-link voltage.
$Z_{b,r}$	Rotor circulating iron impedance.
$Z_{b,s}$	Stator circulating iron impedance.
$Z_{g,s}$	Stator-to-ground impedance.
δ_{Fe}	Skin depth in lamination sheets.
$\frac{du}{dt}$	Voltage slew rate.
μ_0	Magnetic constant.
μ_{Fe}	Lamination relative permeability.
ω_{res}	Angular resonance frequency.
ϕ_{CM}	Common mode flux.
σ_{Fe}	Lamination conductivity.
f_{res}	Resonance frequency.
h_s	Slot height.
i_{CM}	Common mode current.
i_b	Circulating bearing current.
l_{Fe}	Lamination stack length.
l_b	Stack-to-housing distance.
u_{CM}	Common mode voltage.
u_{sh}	Shaft end-to-end voltage.

References

1. Berhausen, S.; Jarek, T. Analysis of Impact of Design Solutions of an Electric Machine with Permanent Magnets for Bearing Voltages with Inverter Power Supply. *Energies* **2022**, *15*, 4475. [[CrossRef](#)]
2. Binder, A.; Muetze, A. Scaling Effects of Inverter-Induced Bearing Currents in AC Machines. *IEEE Trans. Ind. Appl.* **2008**, *44*, 769–776. [[CrossRef](#)]
3. Magdun, O.; Gemeinder, Y.; Binder, A. Rotor impedance of the high frequency circulating bearing current path in inverter-fed AC machines. In Proceedings of the 2013 IEEE Energy Conversion Congress and Exposition, Denver, CO, USA, 15–19 September 2013; pp. 3512–3519. [[CrossRef](#)]
4. Muetze, A.; Binder, A. Calculation of Circulating Bearing Currents in Machines of Inverter-Based Drive Systems. *IEEE Trans. Ind. Electron.* **2007**, *54*, 932–938. [[CrossRef](#)]
5. Yea, M.; Han, K. Modified Slot Opening for Reducing Shaft-to-Frame Voltage of AC Motors. *Energies* **2020**, *13*, 760. [[CrossRef](#)]
6. Schuster, M.; Masendorf, D.; Binder, A. Two PMSMs and the influence of their geometry on common-mode bearing currents. In Proceedings of the 2016 XXII International Conference on Electrical Machines (ICEM), Lausanne, Switzerland, 4–7 September 2016; pp. 2126–2132. [[CrossRef](#)]
7. Jaritz, M.; Jaeger, C.; Bucher, M.; Smajic, J.; Vukovic, D.; Blume, S. An Improved Model for Circulating Bearing Currents in Inverter-Fed AC Machines. In Proceedings of the 2019 IEEE International Conference on Industrial Technology (ICIT), Melbourne, Australia, 13–15 February 2019; pp. 225–230. [[CrossRef](#)]
8. Kindl, V.; Skala, B.; Pechanek, R.; Byrtus, M.; Hruska, K. Calculation of induction machine parasitic capacitances using finite element method. In Proceedings of the 2016 ELEKTRO, Strbske Pleso, High Tatras, Slovakia, 16–18 May 2016; pp. 176–179. [[CrossRef](#)]
9. Sangha, P.; Sawata, T. Evaluation of winding stray capacitance in motors for aerospace applications. In Proceedings of the 2017 IEEE International Electric Machines and Drives Conference (IEMDC), Miami, FL, USA, 21–24 May 2017; pp. 1–6. [[CrossRef](#)]
10. Kim, C.; Jun, S.; Yoon, H.; Kim, N.; Jung, H.; Kim, R.; Jung, S. Calculation of Parasitic Capacitance to Analyze Shaft Voltage of Electric Motor with Direct-Oil-Cooling System. *Processes* **2022**, *10*, 1541. [[CrossRef](#)]
11. Stevic, S.; Tombul, Y.; Lauerburg, M.; Thul, A.; Hameyer, K. Overvoltage Transients in Wide Bandgap-Based Inverter-Fed Variable Speed Electrical Drives. In Proceedings of the PCIM Europe 2022: International Exhibition and Conference for Power Electronics, Intelligent Motion, Renewable Energy and Energy Management, Nuremberg, Germany, 10–12 May 2022; pp. 1–9. [[CrossRef](#)]
12. Moreno, Y.; Almandoz, G.; Egea, A.; Arribas, B.; Urdangarin, A. Analysis of Permanent Magnet Motors in High Frequency—A Review. *Appl. Sci.* **2021**, *11*, 6334. [[CrossRef](#)]
13. Pyrhonen, J.; Jokinen, T.; Hrabovcová, V. *Design of Rotating Electrical Machines*; John Wiley & Sons Ltd.: West Sussex, UK, 2014.
14. Magdun, O.; Binder, A. High-Frequency Induction Machine Modeling for Common Mode Current and Bearing Voltage Calculation. *IEEE Trans. Ind. Appl.* **2014**, *50*, 1780–1790. [[CrossRef](#)]
15. Hanselman, D.C. *Brushless Permanent Magnet Motor Design*; Momentum Press: New York, NY, USA, 2010.
16. Sarrió, J.E.R.; Martis, C.; Chauvicourt, F. Numerical Computation of Parasitic Slot Capacitances in Electrical Machines. In Proceedings of the 2020 International Conference and Exposition on Electrical and Power Engineering (EPE), Iași, Romania, 22–23 October 2020; pp. 146–150. [[CrossRef](#)]
17. Bärnklaue, H.; Harnisch, M.; Proske, J. On Medium Frequency Differential Mode Resonance Effects in Electric Machines. *IEEE Open J. Ind. Appl.* **2021**, *2*, 310–319. [[CrossRef](#)]
18. Zou, T.; Gerada, D.; Rocca, A.L.; Moslem, M.; Cairns, A.; Cui, M.; Bardalai, A.; Zhang, F.; Gerada, C. A Comprehensive Design Guideline of Hairpin Windings for High Power Density Electric Vehicle Traction Motors. *IEEE Trans. Transp. Electr.* **2022**, *8*, 3578–3593. [[CrossRef](#)]

Disclaimer/Publisher’s Note: The statements, opinions and data contained in all publications are solely those of the individual author(s) and contributor(s) and not of MDPI and/or the editor(s). MDPI and/or the editor(s) disclaim responsibility for any injury to people or property resulting from any ideas, methods, instructions or products referred to in the content.